The 28th International Workshop on Active-Matrix Flatpanel Displays and Devices
– TFT Technologies and FPD Materials –
June 29 – July 2, 2021

Gigahertz Large-Area Electronic Devices and Circuits for Wireless Applications

Can Wu*, Yue Ma*, Yoni Mehlman*, Sigurd Wagner, James C. Sturm, Naveen Verma

Princeton University, Department of Electrical and Computer Engineering
Engineering Quadrangle, Olden Street, Princeton, New Jersey, 08544, USA
Phone: +1-609-216-9816 E-mail: canw@princeton.edu

We highlight recent progress in gigahertz large-area electronic (LAE) devices and circuits. On the device level, this relies on advanced design of zinc-oxide (ZnO) thin-film transistors (TFTs), for which we consider three key figures of merit, i.e., unity current gain frequency f_T and unity power gain frequency f_{MAX} of active devices, and unity off-to-on-impedance ratio frequency $f_{cut\text{-}off}$ of passive devices. On the circuit level, this relies on resonant operation and exploiting high-quality-factor LAE inductors. We demonstrate two gigahertz LAE circuits, specifically oscillators and RF switches.

1. Introduction

LAE devices and circuits, which have been employed in flat-panel displays[1,2], have recently drawn interest for broader sensing applications requiring high frequency operation[3,4]. Very recently, this has extended to wireless-sensing applications[5,6,7], where the ratio of radiative aperture dimension (D) to signal wavelength (λ) is critical, as it sets the spatial resolution of a radiating beam. To illustrate the distinct advantage of LAE in such applications compared to Si-CMOS, we compare the achievable aperture sizes (largest D) and operating frequencies (smallest λ) in Fig. 1. While Si-CMOS is capable of operation to hundreds of gigahertz, realistic chip sizes restrict D/λ (typically required to be >10), limiting to applications above 100 GHz frequencies (where circuit power and radiation losses in air[8] are high). On the other hand, bringing LAE into gigahertz regime opens up a new frequency range for large D/λ's ('This work' region in Fig. 1). This frequency band is of interest for long-range wireless communication (cellular phones, satellites) and indoor meters-scale communication (WLAN, Bluetooth). In addition, due to low temperature processing, LAE also enables flexible and conformal form factors, which could ease deployment of wireless nodes in 5G/IoT networks.

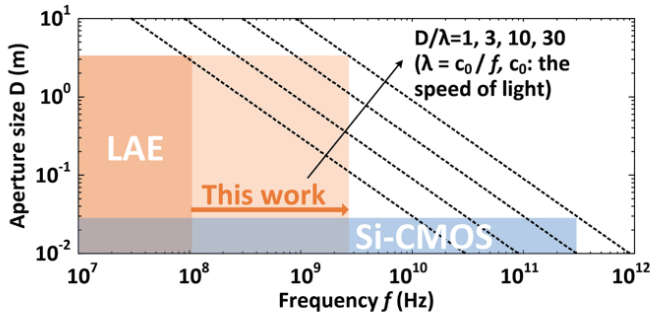

Fig. 1. Aperture size D and frequency f achievable by LAE and Si-CMOS. This work extends LAE from ~100 MHz to gigahertz.

To extend TFT's to the gigahertz regime, we redesigned ZnO-based TFTs, as captured by separate metrics for transistors working as active or as passive devices. Here, we summarize our recent progress for active devices, as measured by the achieved unity current gain (f_T) and unity power gain frequencies (f_{MAX}), and then for passive devices, as measured by the achieved unity off-to-on-impedance ratio frequency ($f_{cut\text{-}off}$, defined later). Using the enhanced LAE TFTs, we demonstrate two LAE circuits: (1) a 1.25 GHz oscillator; and (2) a 2.4 GHz resonant RF switch.

2. Device design

Fig. 2 shows our bottom-gate ZnO TFTs processed at <200 °C[9]; its DC characteristics are shown in Fig. 3.

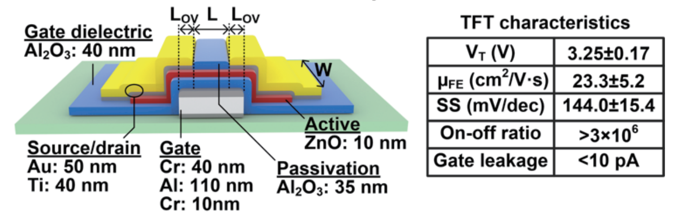

TFT characteristics	
V_T (V)	3.25±0.17
μ_{FE} (cm^2/V·s)	23.3±5.2
SS (mV/dec)	144.0±15.4
On-off ratio	>3×10^6
Gate leakage	<10 pA

Fig. 2. Left: schematic of the ZnO TFTs employed in this work. Al_2O_3 and ZnO are deposited by plasma-enhanced atomic layer deposition (PEALD). Right: extracted DC parameters.

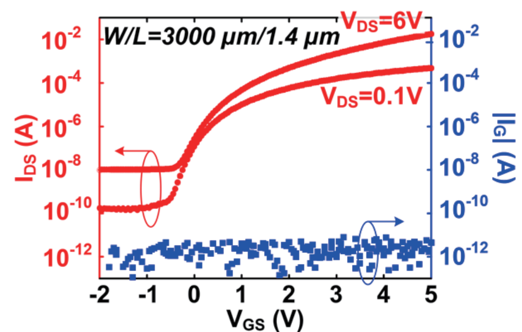

Fig. 3. Measured I_{DS}–V_{GS} transfer curve of ZnO TFT.

*These authors contributed equally.

ISBN 978-4-9912169-0-9 ©2021 FTFMD

Authorized licensed use limited to: Princeton University. Downloaded on August 21,2024 at 17:00:04 UTC from IEEE Xplore. Restrictions apply.

A. f_T and f_{MAX} of an active device

Fig. 4 shows a small-signal circuit model for the TFT as an active device biased in the saturation regime. f_T and f_{MAX} can be estimated with the following well-known expressions:

$$f_T = \frac{g_m}{2\pi(C_{GD}+C_{GS})}; \quad (1)$$

$$f_{MAX} = \frac{f_T}{2\sqrt{R_G(2\pi f_T C_{GD}+1/r_0)}}. \quad (2)$$

Both f_T and f_{MAX} depend on capacitances C_{GD} and C_{GS}, and transconductance g_m, hence ultimately, on device geometry and charge-carrier mobility. In addition, f_{MAX} depends on gate resistance R_G. Fig. 5 illustrates how f_T and f_{MAX} scale with the device geometries, with the assumption that low-resistance gate metal is used (R = 2Ω/square).

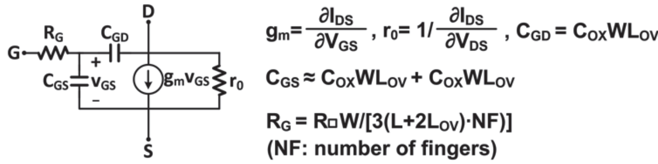

Fig. 4. Small-signal circuit model of a TFT as an active device biased in the saturation regime.

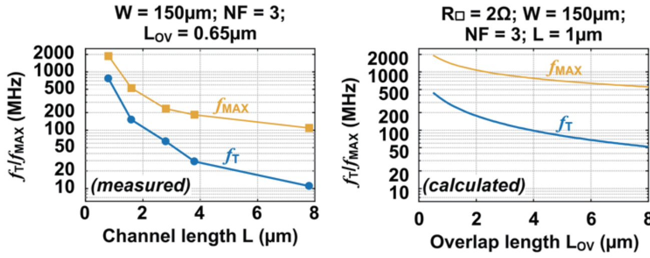

Fig. 5. Measured and calculated f_T and f_{MAX} vs. channel length L, and gate-drain and gate-source overlap length L_{OV}.

To enhance f_T and f_{MAX}, we: (1) scale the channel length down to 1μm; (2) reduce the G-S/D overlaps to ~0.5μm using a self-aligned process; and (3) minimize the gate resistance by depositing a thick composite metal stack (Cr/Al/Cr = 10nm/110nm/40nm, as shown in Fig. 2) and employing a multi-finger layout[9]. Fig. 6 illustrates the self-aligning process step and shows an SEM image of the TFT channel region. As shown in Fig. 7, we measure the current gain ($|H_{21}|$) and maximal available gain (MAG) for our ZnO TFTs. f_T and f_{MAX} are extracted to be 420 MHz and 2 GHz. Other works also achieve similar or comparable f_T/f_{MAX} in LAE IGZO TFTs[10,11].

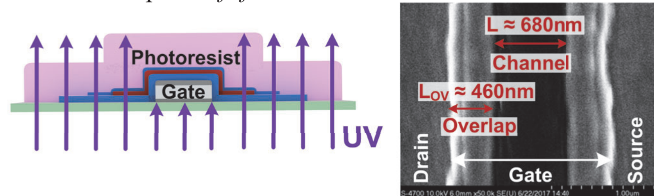

Fig. 6. Left: TFT S/D metal patterning, self-aligned to gate by backside exposure. Right: SEM image of the TFT channel region. L ≈ 680nm; L_{OV} ≈ 460nm.

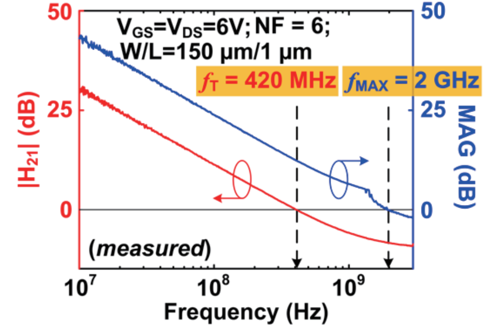

Fig. 7. Measured current gain ($|H_{21}|$) and maximal available power gain (MAG) vs. frequency.

Note that f_{MAX} can be made significantly higher than f_T, because of dependence on R_G, which can be reduced by including a thick Al layer in the gate electrode stack (Fig. 2). This motivates LAE circuits that are f_{MAX}-limited rather than f_T-limited.

B. $f_{cut\text{-}off}$ of a passive device

Fig. 8 shows a circuit model for the TFT as a passive RF switch biased in the linear regime. The off-state impedance is dominated by the drain/source-to-gate overlap capacitance, i.e., $C_{GD}||C_{GS}$, and thus inversely proportional to frequency, while the on-state is dominated by the channel resistance R_{CH}. Hence, the cut-off frequency is defined as the frequency where the off-state impedance becomes equal to the on-state impedance, i.e.,

$$f_{cut-off} \approx \frac{1}{2\pi R_{CH}(C_{GD}||C_{GS})}. \quad (3)$$

Beyond $f_{cut\text{-}off}$ the switch loses impedance control (the switch impedance does not depend on the gate voltage).

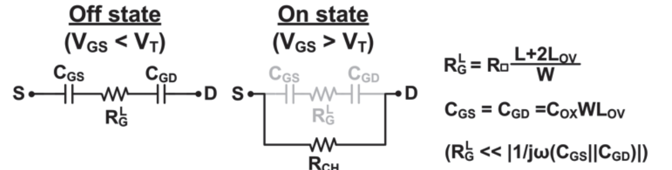

Fig. 8. Circuit model for the TFT as a passive switch. While the off-state conductance is set by the parasitic conduction path C_{GD}-R_G^L-C_{GS}, the on state is dominated by R_{CH}. $R_G^L = R \cdot (L+2L_{OV})/W$ denotes the gate resistance in the channel length direction, which differs from the R_G in Fig. 4.

Note that the $f_{cut\text{-}off}$ expression is based on the assumption that $R_G^L \ll |1/j\omega(C_{GD}||C_{GS})|$. It might at first appear that the parasitic conduction path (C_{GD}-R_G^L-C_{GS}) in the off state can be eliminated by using a highly resistive gate, thereby raising $f_{cut\text{-}off}$. However, this approach would introduce a large resistance along the gate-bias feed line, leading to an excessive time constant (~milliseconds) for switching the gate; practical wireless applications require ~nanoseconds switching, making excessive R_G^L unacceptable. Note that the gate terminal is made AC-open by placing a high-valued resistor in series with the gate-bias feed line, to prevent the DC biasing traces from creating parasitic RF paths.

Authorized licensed use limited to: Princeton University. Downloaded on August 21,2024 at 17:00:04 UTC from IEEE Xplore. Restrictions apply.

Guided by the $f_{cut\text{-}off}$ expression, we raise $f_{cut\text{-}off}$ by: (1) reducing the overlap capacitance (C_{GS} and C_{GD}) via the self-aligned process illustrated in Fig. 6; and (2) minimizing R_{CH} via aggressive gate biasing[7], e.g., V_{GS}=20V. A study of the breakdown conditions of our ZnO TFTs[7] identified the operating regime where high V_{GS} can be applied. Fig. 9 shows an inverse relation of V_{DS} and breakdown current $I_{DS,BREAK}$, such that the breakdown power $P_{BREAK}=V_{DS} \cdot I_{DS,BREAK}$ is roughly constant. This suggests thermally-induced breakdown. A key attribute of a passive switch is its deep-triode operation, i.e., low V_{DS}, in contrast to active devices biased into saturation regime. The constant breakdown power ($P_{BREAK}=V_{DS}^2/R_{CH}$) suggests that at low V_{DS}, V_{GS} can be safely set to high values, to reduce R_{CH}. Fig. 10 shows measured on-state and off-state impedances at three different V_{GS}. As seen, pushing V_{GS} to 20V (in combination with self-alignment) boosts $f_{cut\text{-}off}$ to 7.2 GHz. while ensuring an adequate margin against TFT breakdown.

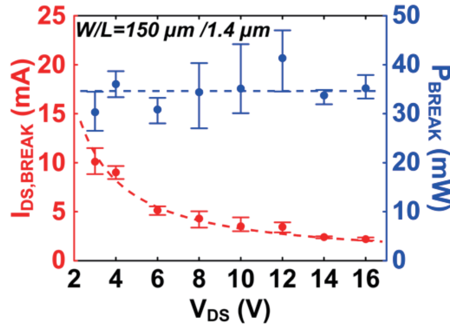

Fig. 9. Measured breakdown current $I_{DS,BREAK}$ vs. V_{DS}, and breakdown power $P_{BREAK} = I_{DS,BREAK} \cdot V_{DS}$ vs. V_{DS}.

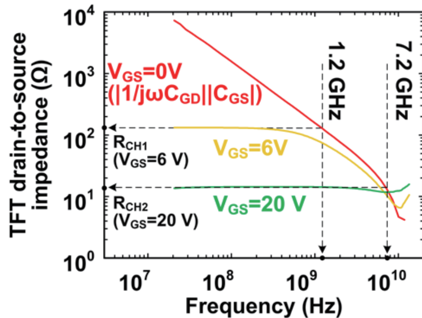

Fig. 10. Measured ZnO TFT impedances at V_{GS} = 0V, 6V, and 20 V. W / L = 3000μm / 1.4μm.

3. Gigahertz LAE circuits demonstrations

Using the devices developed above, we demonstrate two exemplary circuits at gigahertz frequencies.

A. Oscillator at 1.25 GHz

Oscillators serving as high-frequency signal generators are essential components in RF systems. Fig. 11 shows our design for a cross-coupled inductor-capacitor (LC) oscillator[12]; capacitors C and resistors R represent parasitic capacitances and losses in the circuit. The key to this topology in LAE is: (1) resonant operation makes it f_{MAX}, rather the f_T limited; and (2) it exploits the ability to create high-quality-factor LAE inductors[13]. High quality-factor planar-spiral inductors are possible in LAE, thanks to large dimensions, thick metal traces, and low-loss substrates.

To sustain oscillations, a positive feedback with loop phase of 0º and gain larger than unity must be established. These are achieved by: (1) a phase shift of 0º provided by the RLC networks at their resonant frequency $1/2\pi\sqrt{LC}$; (2) a loop gain of $(g_m R)^2$>1, realized by properly sizing the inductor and the TFTs. To maximize the loop gain, we perform the following optimization:

$$\arg\max\,(g_m R)^2$$
$$\text{subject to } \frac{1}{2\pi\sqrt{LC}} = \text{target frequency (i.e., 1.25 GHz)}. \quad (4)$$

Note that g_m, R, L, and C depend on inductor and TFT sizes. The resulting parameters are shown in Fig. 11, which produce a gain of ~2.6, leaving adequate margin for device variations.

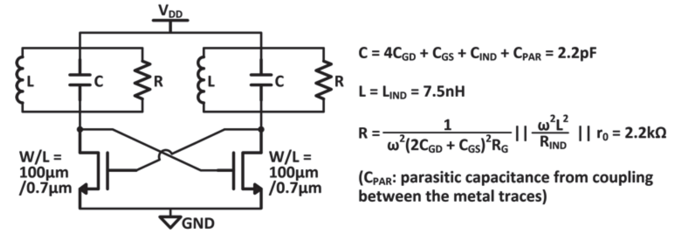

Fig. 11. Schematic of the cross-coupled LC oscillator circuit, and the parameters that produce maximal loop gain.

Fig. 12 shows our prototyped oscillator. To enhance testability, we integrate it on a PCB with auxiliary circuits for signal monitoring (voltage buffer) and supplying power (voltage regulator). The inductor is implemented as a planar loop on the PCB, made of copper with a radius of 4mm, a line width of 1mm and a thickness of 35μm. The captured time-domain waveform is shown in Fig. 13. Its frequency transform indicates an oscillation frequency of 1.25 GHz.

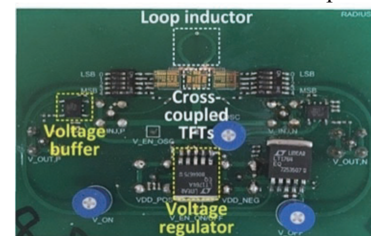

Fig. 12. Integrated oscillator on PCB.

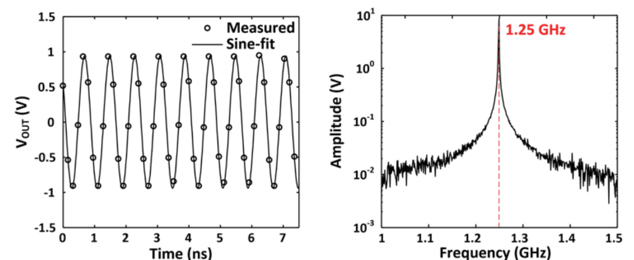

Fig. 13. Left: time-domain waveform of the oscillator output voltage. Right:

ISBN 978-4-9912169-0-9 ©2021 FTFMD
Authorized licensed use limited to: Princeton University. Downloaded on August 21,2024 at 17:00:04 UTC from IEEE Xplore. Restrictions apply.

FFT results.

B. Resonant RF switch at 2.4 GHz

RF switches, used for routing RF signals, are an equally critical component of many RF systems. However, the off-to-on impedance ratio of the TFT with $f_{cut\text{-}off}$ of 7.2 GHz of Section 2 (Fig. 10) is not sufficiently high for practical use, at target frequencies of 2.4 GHz (typical for wireless sensing applications).

We employ resonant operation to raise the impedance ratio. A planar inductor is put in parallel with the TFT to resonate out the parasitic capacitors ($C_{GS}||C_{GD}$)[7]. The result, shown in Fig. 14, is an off impedance that ultimately is limited by the quality factors of the capacitance branch (i.e., $1/(|j\omega C_{GD}||C_{GS}|) / R_G^L$) and the inductor branch (i.e., $|j\omega L_{IND}| / R_{IND}$). To minimize R_G^L and R_{IND}, we employ: (1) the thick, composite gate metal shown in Fig. 2; and (2) an on-chip loop inductor made of gold, with 1mm radius, 200µm trace width, and 2.5µm thickness (≈ skin depth at 2.4 GHz).

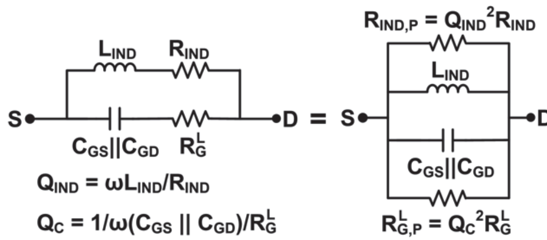

Fig. 14. Circuit model for the resonant RF switch in the off state.

Fig. 15 shows the resonant switch fabricated on glass. A ~20 kΩ resistor made of 15 nm-thick Cr film is put in series with the gate to prevent the DC biasing traces from creating parasitic RF paths, and to protect the TFTs from ESD damage. Within the frequency band centered at 2.4 GHz (±200 MHz) the measured switch impedance ratio ranges from 22 to 48. In effect, this resonant operation trades in bandwidth for impedance ratio. This is a practical approach for many RF wireless systems in the 2.4 GHz band, where narrow-band operation often is chosen for energy efficiency.

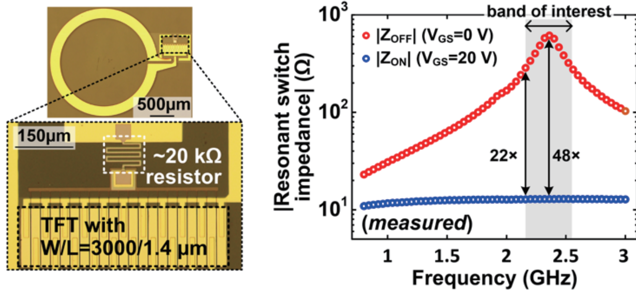

Fig. 15. Left: microscope image of the resonant RF switch fabricated on glass, with zoom-in on the TFT and the ~20 kΩ resistor for gate DC bias. Right: measured impedances of the resonant RF switch in its off and on state, at V_{GS} = 0V and 20V, respectively.

4. Conclusions

Gigahertz LAE TFTs were designed and fabricated for active and passive applications, with f_T of 420 MHz, f_{MAX} of 2 GHz, and $f_{cut\text{-}off}$ of 7.2 GHz. Oscillator circuits at 1.25 GHz and resonant RF switches operating at 2.4 GHz were developed. These are fundamental building blocks for LAE RF systems. We believe this work opens a path towards gigahertz LAE in wireless applications, which will combine 2.4 GHz-compatible D/λ with monolithic integration, and flexible/conformal form factors.

Acknowledgments

This work was supported by grants from Semiconductor Research Corporation (SRC), DARPA, and the Princeton Program in Plasma Science and Technology (PPST). The Princeton PRISM cleanroom facilities were used for this project.

References

1. S. Chen, et al. *Active-matrix organic light-emitting display technologies*. (Bentham Science Publishers, 2015).
2. D. B. Willem. *Active matrix liquid crystal displays: fundamentals and applications*. (Elsevier, 2011).
3. N. Verma, et al., *Proc. IEEE* **103**, 690–712 (2015).
4. M. Ozatay, et al., in *2018 IEEE Custom Integrated Circuits Conference 1-8 (CICC)* (2018).
5. H. Subbaraman, et al., *IEEE Antennas Wirel. Propag. Lett.* **12**, 170–173 (2013).
6. L. Huang, et al., in *2013 IEEE International Solid-State Circuits Conference* 458–459 (2013).
7. C. Wu, et al., in *2020 IEEE International Electron Devices Meeting (IEDM)* 741–744 (2020).
8. S. Rangan, et al., *Proc. IEEE* **102**, 366–385 (2014).
9. Y. Mehlman, et al., in *75th Device Research Conference (DRC) 1-2* (2017).
10. N. Münzenrieder, et al., *IEEE Trans. Electron Devices* **60**, 2815–2820 (2013).
11. U. Kalita, et al., *IEEE Microw. Wirel. Components Lett.* **29**, 119–121 (2019).
12. Y. Mehlman, et al., in *77th Device Research Conference (DRC)* 63–64 (2019).
13. Y. Hu, et al., in *2012 IEEE Cust. Integr. Circuits Conf.* 1–4 (2012).

Authorized licensed use limited to: Princeton University. Downloaded on August 21,2024 at 17:00:04 UTC from IEEE Xplore. Restrictions apply.